Showcasing research from Professor Guangjin Zhang's laboratory, Institute of Process Engineering, Chinese Academy of Sciences, Beijing, China.

Electrochemical C–N coupling with perovskite hybrids toward efficient urea synthesis

In this work, Zhang *et al.* proposed a unique ultrasonic bath method to fabricate perovskite structural $BiFeO_3/BiVO_4$ hybrids. The local charge redistribution in $BiFeO_3/BiVO_4$ hybrids promotes the targeted adsorption and activation of inert N_2 and CO_2 molecules and further electrochemical C-N coupling reactions to form urea with high efficiency. The authors appreciate the help from Chinese artist, Miss Lina Zhao, for the designing of this cover image.

As featured in:

See Guangjin Zhang *et al.*, *Chem. Sci.*, 2021, **12**, 6048.

ROYAL SOCIETY OF CHEMISTRY

rsc.li/chemical-science

Registered charity number: 207890

Chemical Science

ROYAL SOCIETY OF CHEMISTRY

EDGE ARTICLE

View Article Online
View Journal | View Issue

Check for updates

Cite this: *Chem. Sci.*, 2021, **12**, 6048

All publication charges for this article have been paid for by the Royal Society of Chemistry

Open Access Article. Published on 12 April 2021. Downloaded on 09/11/2024 10:38:50 AM.
This article is licensed under a Creative Commons Attribution 3.0 Unported Licence.

Electrochemical C–N coupling with perovskite hybrids toward efficient urea synthesis†

Menglei Yuan,[ab] Junwu Chen,[ab] Yiling Bai,[cd] Zhanjun Liu,[c] Jingxian Zhang,[ab] Tongkun Zhao,[ab] Qiaona Shi,[e] Shuwei Li,[a] Xi Wang [fg] and Guangjin Zhang *[abg]

Received 13th March 2021
Accepted 11th April 2021

DOI: 10.1039/d1sc01467f

rsc.li/chemical-science

Electrocatalytic C–N coupling reaction by co-activation of both N_2 and CO_2 molecules under ambient conditions to synthesize valuable urea opens a new avenue for sustainable development, while the actual catalytic activity is limited by poor adsorption and coupling capability of gas molecules on the catalyst surface. Herein, theoretical calculation predicts that the well-developed built-in electric field in perovskite hetero-structured $BiFeO_3/BiVO_4$ hybrids can accelerate the local charge redistribution and thus promote the targeted adsorption and activation of inert N_2 and CO_2 molecules on the generated local electrophilic and nucleophilic regions. Thus, a $BiFeO_3/BiVO_4$ heterojunction is designed and synthesized, which delivers a urea yield rate of 4.94 mmol h^{-1} g^{-1} with a faradaic efficiency of 17.18% at −0.4 V *vs.* RHE in 0.1 M $KHCO_3$, outperforming the highest values reported as far. The comprehensive analysis further confirms that the local charge redistribution in the heterojunction effectively suppresses CO poisoning and the formation of the endothermic *NNH intermediate, which thus guarantees the exothermic coupling of *N=N* intermediates with the generated CO *via* C–N coupling reactions to form the urea precursor *NCON* intermediate. This work opens a new avenue for effective electrocatalytic C–N coupling under ambient conditions.

1 Introduction

Nitrogen (N_2), accounting for 78% of the atmosphere, exists in the gaseous form that can't be directly utilized in biology and chemistry fields.[1–3] On the other hand, carbon dioxide (CO_2) generated from industries and transportation is the principal greenhouse gas causing serious environmental concerns.[4–8] Thus, converting N_2 and CO_2 into value-added fuels and chemical products *via* the C–N coupling reaction is a promising approach for not only mitigating environmental issues and energy crisis but also high-value utilization of N_2 and CO_2.[9–12] However, the highly stable double-bond (C=O, 806 kJ mol^{-1}) in CO_2 molecules and the triple-bond (N≡N, 940.95 kJ mol^{-1}) in N_2 molecules make the inert gas molecules difficult to activate mildly.[13–17] Although conventional industrial processes such as the Haber–Bosch method and carbon capture and sequestration achieve the activation of inert gas molecules, their further utilization is impeded by the large energy consumption and complex synthetic processes.[18–22] In comparison, energy-saving and environmentally benign electrocatalysis technologies such as the nitrogen reduction reaction (NRR) and the carbon dioxide reduction reaction (CO_2RR) are drawing growing attention.[23–30] Besides, the emerged electrochemical C–N coupling reaction may provide a new possibility of enhancing the spectrum of products of CO_2 by using CO_2 and amine derivatives/nitrogen sources (nitrate, nitrite, NO, and even N_2) as feedstock.[9,31,32]

The desired product urea [$CO(NH_2)_2$] will be produced when the electrochemical C–N bond formation occurs by employing both N_2 and CO_2 as the feeding gas.[9] Urea is commonly utilized as the general feedstock in industry and the primary fertilizer for agriculture.[33,34] The industrial urea synthesis proceeds by two consecutive processes, including $N_2 + H_2 \rightarrow NH_3$ followed by $NH_3 + CO_2 \rightarrow CO(NH_2)_2$, which operate under harsh reaction conditions (350–550 °C, 150–350 bar and 150–200 °C, 150–250 bar, respectively).[35] Compared with the complex industrial synthetic process, simultaneous electrocatalytic fixation of N_2 and CO_2 driven by a renewable energy source under ambient

[a]*CAS Key Laboratory of Green Process Engineering, Beijing Key Laboratory of Ionic Liquids Clean Process, State Key Laboratory of Multiphase Complex Systems, Institute of Process Engineering, Chinese Academy of Sciences, Beijing, 100190, China. E-mail: zhanggj@ipe.ac.cn*

[b]*Center of Materials Science and Optoelectronics Engineering, University of Chinese Academy of Sciences, Beijing, 100049, China*

[c]*State Key Laboratory of Coal Conversion, CAS Key Laboratory of Carbon Materials, Institute of Coal Chemistry, Chinese Academy of Sciences, Taiyuan, 030001, China*

[d]*SynCat@Beijing, Synfuels China Technology Co. Ltd., Huairou District, Beijing, 101407, China*

[e]*Sino Shaanxi Nuclear Molybdenum Industry Co. Ltd., Tongguan, 714300, China*

[f]*Key Laboratory of Luminescence of Optical Information, Ministry of Education, Beijing Jiaotong University, Beijing, 100044, China*

[g]*Chemistry and Chemical Engineering Guangdong Laboratory, Shantou, 515031, China*

† Electronic supplementary information (ESI) available. See DOI: 10.1039/d1sc01467f

© 2021 The Author(s). Published by the Royal Society of Chemistry

Open Access Article. Published on 12 April 2021. Downloaded on 09/11/2024 10:38:50 AM.
This article is licensed under a Creative Commons Attribution 3.0 Unported Licence.

conditions provides a clean route for urea production.[9] The main issues in electrochemical synthesis of urea lie in three aspects: (1) extraordinarily weak chemical adsorption of inert CO_2/N_2 on the catalysts surface;[29,30,36,37] (2) the dissociation of the highly stable C═O bond and N≡N bond requires high overpotential;[13,15] (3) the parallel reaction of CO_2/N_2 reduction suppresses the efficiency of C–N coupling and strongly competes with the desired urea formation reaction, further resulting in a large distribution of complex products.[9]

Although a few noble metal Pd-based catalysts can achieve urea electrosynthesis, the related catalytic activity showed a maximum urea yield rate of 3.36 mmol h^{-1} g^{-1} with a FE of 8.92%.[9] Besides, the high price and scarcity of the used noble metals impede their real application on the large scale. Thus, further improvement of the catalytic activity with earth-abundant materials remains a challenge. Inspired by the different electronic structures of N_2 and CO_2 molecules, tuning the electronic state of the electrocatalyst's surface can be a feasible strategy to optimize the adsorption of reactant gas molecules and suppress the competing electro-reduction reactions to promote urea generation. In this regard, fabricating a built-in electronic field to accelerate the local charge redistribution in perovskite heterostructures displays fascinating potential to deliver impressive urea electroproduction activity. On the one hand, perovskite structured transition-metal oxide (ABO_3) semiconductors possess a distinctive electronic structure, which can lead to the alteration of electron density when combining with other domains.[38,39] On the other hand, the work function difference in perovskite heterostructures drives the local charge redistribution by the band bending at the heterointerface, which is preferred for targeted adsorption and activation of inert small molecules such as N_2, CO_2, H_2O, and so on.[40] Despite the encouraging merits, inducing the local charge redistribution in perovskite hybrids toward the specific urea electrosynthesis hasn't been explored.

In this work, with the aid of theoretical simulation, we exploited perovskite structured p-type $BiFeO_3$ and an n-type semiconductor $BiVO_4$ to fabricate innovative p–n heterojunction electrocatalysts, aiming at enabling spontaneous electron transfer at the heterointerfaces by the desirable built-in electric field. The obtained perovskite structured $BiFeO_3$/$BiVO_4$ showed high electrocatalytic activity toward the C–N coupling reaction to synthesize urea, and exhibits a FE of 17.18% in 0.1 M $KHCO_3$ at −0.4 V *vs.* RHE. The urea yield rate can reach 4.94 mmol h^{-1} g^{-1} which is much higher than the recently reported best values with Pd-based electrocatalysts. The activity can further be improved by adding an ionic liquid to the electrolyte. The generated local electrophilic and nucleophilic regions enhanced the targeted adsorption and activation of inert N_2 and CO_2 molecules and balanced the competing electro-reduction reactions to further promote the formation of the *NCON* intermediate *via* the C–N bond coupling reaction. Thus, engineering a built-in electric field to facilitate local charge redistribution has been proposed as an appealing strategy to enhance electrocatalytic C–N bond coupling and further urea synthesis.

2 Results and discussion

Conspicuously, the charged surface can give rise to a significant effect on the targeted adsorption of reactant molecules.[30] In this regard, constructing built-in fields at the heterointerface to promote a spontaneous electron transfer process will supply more possibilities for generating desirable two opposite charged regions.[41] This design concept has been confirmed by the investigation of various perovskite-based semiconductor catalysts, which can constitute distinct p–n junctions and thus accelerate local charge redistribution at the heterointerface.[40] The band theory of solids has confirmed that the behavior of electron transfer is strongly correlated to the work function of semiconductors.[42] As presented in Fig. 1a and b, the theoretical simulation results showed that the work function values of $BiVO_4$ and $BiFeO_3$ were 3.23 eV and 6.30 eV, respectively, which allow self-driven electron transfer from $BiVO_4$ to $BiFeO_3$. The profile of the planar averaged electrostatic potential along the *z*-direction for $BiFeO_3$/$BiVO_4$ hybrids is depicted in Fig. 1c. Compared with pristine $BiVO_4$ and $BiFeO_3$ that possess periodic lattice potential, $BiFeO_3$/$BiVO_4$ hybrids showed a big build-in potential at the interfaces. Additionally, electron density difference calculation was further performed to reveal the charge distribution at the interface of $BiFeO_3$/$BiVO_4$ hybrids. As described in Fig. 1d, the charge depletion and accumulation are represented by the cyan region and yellow region, respectively. An increase of the charge density was observed at the $BiFeO_3$ surface and a decrease at the $BiVO_4$ surface, which confirmed that the spontaneous electron transfer induced the local charge redistribution around the interface and endowed the surfaces of $BiFeO_3$ and $BiVO_4$ with local nucleophilic and electrophilic regions. Bader analysis results further demonstrate that $BiVO_4$ can transfer 2.33 electrons to $BiFeO_3$. Previous research has proven that the chemisorption of inert CO_2 and N_2 is the initial step for electrocatalytic urea production. As shown in Fig. S1,† the N atom in the N_2 molecule and the C atom in the CO_2 molecule are electron-rich and electron-deficient, respectively. Therefore, it can be deduced that the rationally designed $BiFeO_3$/$BiVO_4$ hybrids with local nucleophilic and electrophilic regions would adsorb targeted reactant molecules by electrostatic interaction. To confirm the above hypothesis, density functional theory (DFT) calculations were performed to reveal the gas adsorption behavior on the surface of the electrocatalyst. As expected, the calculated adsorption energies of $BiFeO_3$/$BiVO_4$ hybrids for N_2 and CO_2 are −0.17 eV and −0.06 eV, much lower than those of individual architectures of $BiFeO_3$ and $BiVO_4$ (Fig. 1e and f), proving that N_2 and CO_2 show a stronger tendency to adsorb on the surface of $BiFeO_3$/$BiVO_4$ hybrids than on pristine $BiFeO_3$ and $BiVO_4$ due to the interfacial interaction triggered by the well-defined space-charge region, which is favorable for much readily chemisorbing inert gas molecules and thus facilitating the electrocatalytic urea production process.

As a proof-of-concept experiment, perovskite structured $BiFeO_3$/$BiVO_4$ hybrids were designed and synthesized by the facile ultrasonic bath method. The field-emission scanning

Open Access Article. Published on 12 April 2021. Downloaded on 09/11/2024 10:38:50 AM.
This article is licensed under a Creative Commons Attribution 3.0 Unported Licence.

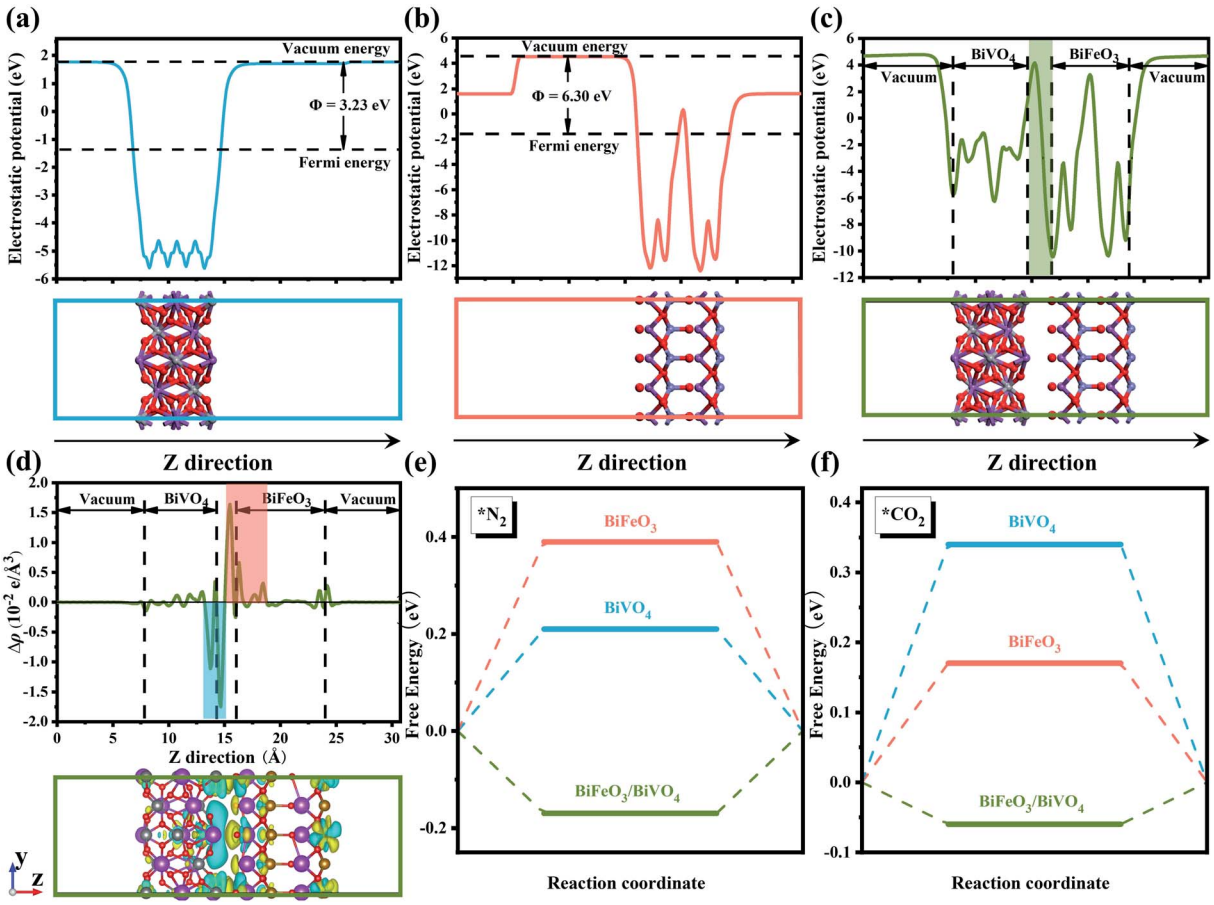

Fig. 1 The calculated electrostatic potentials and work functions for (a) $BiVO_4$, (b) $BiFeO_3$ and (c) $BiFeO_3/BiVO_4$ heterojunction surfaces; (d) planar average charge density difference along the *z*-direction for the $BiFeO_3/BiVO_4$ heterojunction, the bottom image shows the charge density difference of the $BiFeO_3/BiVO_4$ heterojunction, the yellow and cyan color indicate electron accumulation and depletion, respectively, with an isosurface value of 0.013 e $Å^{-3}$; free energy diagrams for (e) N_2 and (f) CO_2 adsorption on $BiFeO_3$, $BiVO_4$ and the $BiFeO_3/BiVO_4$ heterojunction.

electron microscopy (FE-SEM) image in Fig. 2a reveals that $BiFeO_3/BiVO_4$ heterostructures possess a rice-like morphology with an average length of 1 μm and a diameter of approximately 400 nm, respectively. The relevant elemental mapping demonstrates the evenly distributed Bi, Fe, V, and O elements. In comparison, pristine $BiVO_4$ still maintains the same morphology as heterostructured hybrids (Fig. 2c), whereas the $BiFeO_3$ displays an irregular nanoparticle structure (Fig. 2b). As surveyed by high-resolution transmission electron microscopy (HR-TEM), the well-resolved lattice fringes of 0.282 nm and 0.312 nm corresponded to the (104) plane and (130) plane of $BiFeO_3$ and $BiVO_4$ crystals (Fig. 2e). Meanwhile, the distinct interface generated by the intimate contact of $BiFeO_3$ and $BiVO_4$ confirms the representative establishment of nanoscale heterostructures (Fig. 2d).

In Fig. 3a and b, the XRD spectra show that the hexagonal $BiFeO_3$ structure (JCPDS: 86-1518) and monoclinic $BiVO_4$ phase (JCPDS: 83-1700) can be obtained in pristine $BiFeO_3$ and $BiVO_4$ samples. Concerning $BiFeO_3/BiVO_4$ hybrids, both sets of diffraction peaks are consistent with those of pristine samples, except for the slight shift of the characteristic peaks of $BiFeO_3$ and partial peaks of $BiVO_4$ to higher diffraction angles (Fig. 3c), which indicates the possible interaction between the two distinct domains.[43,44] As further revealed by Mott–Schottky (M–S) curves, $BiFeO_3$ with a negative slope (Fig. 3d) and $BiVO_4$ with a positive slope (Fig. 3e) matched well with the apparent characteristics of a p-type and an n-type semiconductor, respectively. In comparison, the as-prepared $BiFeO_3/BiVO_4$ hybrids exhibited evident p–n heterojunction features (Fig. 3f), which furnish the rational architecture to achieve the desired local charge redistribution by the above theoretical prediction. In Raman spectra (Fig. 4a), the typical vibrational bands at 137 and 171 cm^{-1} represent the Fe–O–Fe bonds of the $BiFeO_3$ sample,[45,46] whereas they exhibit a slightly negative shift accompanied by an intensity decrease when coupled with $BiVO_4$ domains. Likewise, the detected V–O stretching modes (637, 702, and 826 cm^{-1}) and VO_4^{3-} tetrahedron bending modes (327 and 367 cm^{-1}) also negatively shifted after the establishment of the heterostructure with the space-charge region.[47–49] This broadening of vibrational modes and position shifting in $BiFeO_3/BiVO_4$ hybrids manifest the intense coupling interaction between $BiFeO_3$ and $BiVO_4$.[50,51] Besides, compared to the UV-Vis spectrum of pristine samples, the dominant peak in $BiFeO_3/BiVO_4$ hybrids exhibited an obvious blue shift, evidencing the

© 2021 The Author(s). Published by the Royal Society of Chemistry

Open Access Article. Published on 12 April 2021. Downloaded on 09/11/2024 10:38:50 AM.
This article is licensed under a Creative Commons Attribution 3.0 Unported Licence.

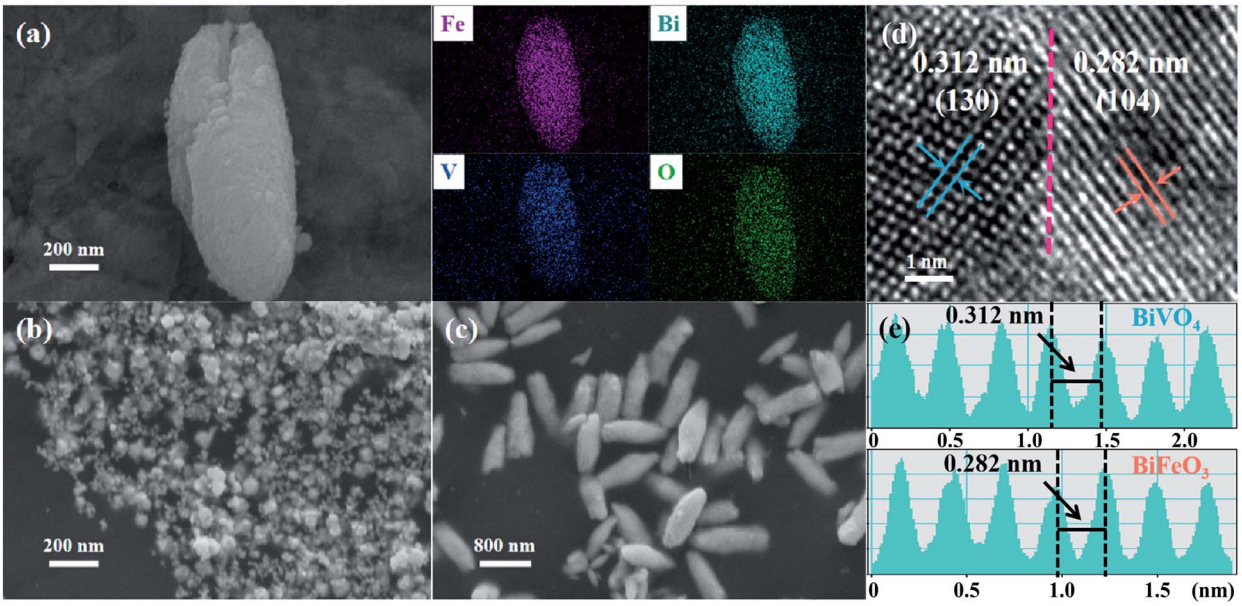

Fig. 2 (a) SEM image and the corresponding elemental mapping of $BiFeO_3/BiVO_4$ hybrids; SEM images of (b) $BiFeO_3$ and (c) $BiVO_4$; (d) high-resolution TEM image of $BiFeO_3/BiVO_4$ hybrids and the dotted line represents the heterointerfaces; (e) the well-resolved lattice fringe of $BiFeO_3/BiVO_4$ hybrids in Fig. 2d.

existence of the charge transfer effect (Fig. 4b).[52] To further reveal the electronic effects between $BiFeO_3$ and $BiVO_4$, the chemical components and the alteration of valence states in the formed catalysts were further examined by X-ray photoelectron spectroscopy (XPS). The survey spectra, displayed in Fig. 4c, illustrate the presence of Bi, Fe, V, and O elements in the obtained electrocatalysts, which is consistent with the above SEM characterization. The high-resolution Bi 4f spectrum displayed two predominant peaks of Bi^{3+} $4f_{7/2}$ and Bi^{3+} $4f_{5/2}$ at the binding energies of 159.3 eV and 164.7 eV (Fig. 4d).[53,54]

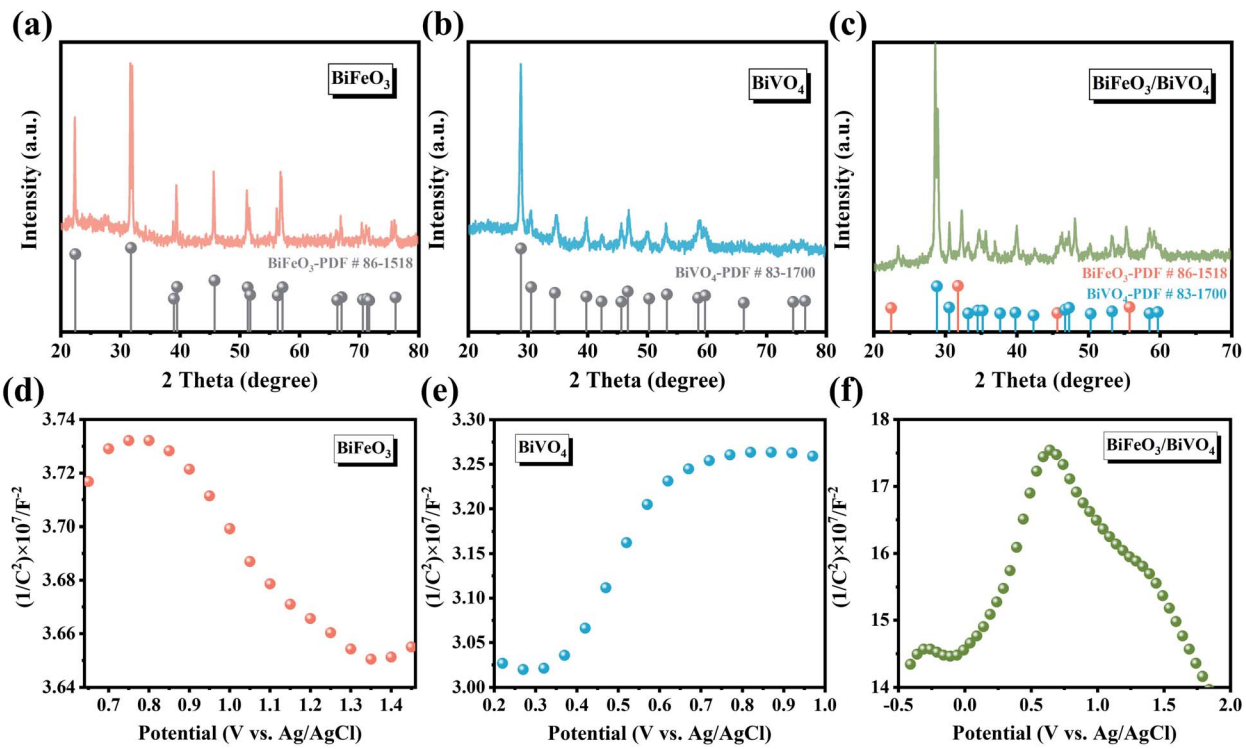

Fig. 3 XRD patterns of (a) $BiFeO_3$, (b) $BiVO_4$ and (c) $BiFeO_3/BiVO_4$; Mott–Schottky plots of (d) $BiFeO_3$, (e) $BiVO_4$ and (f) $BiFeO_3/BiVO_4$.

Open Access Article. Published on 12 April 2021. Downloaded on 09/11/2024 10:38:50 AM.
This article is licensed under a Creative Commons Attribution 3.0 Unported Licence.

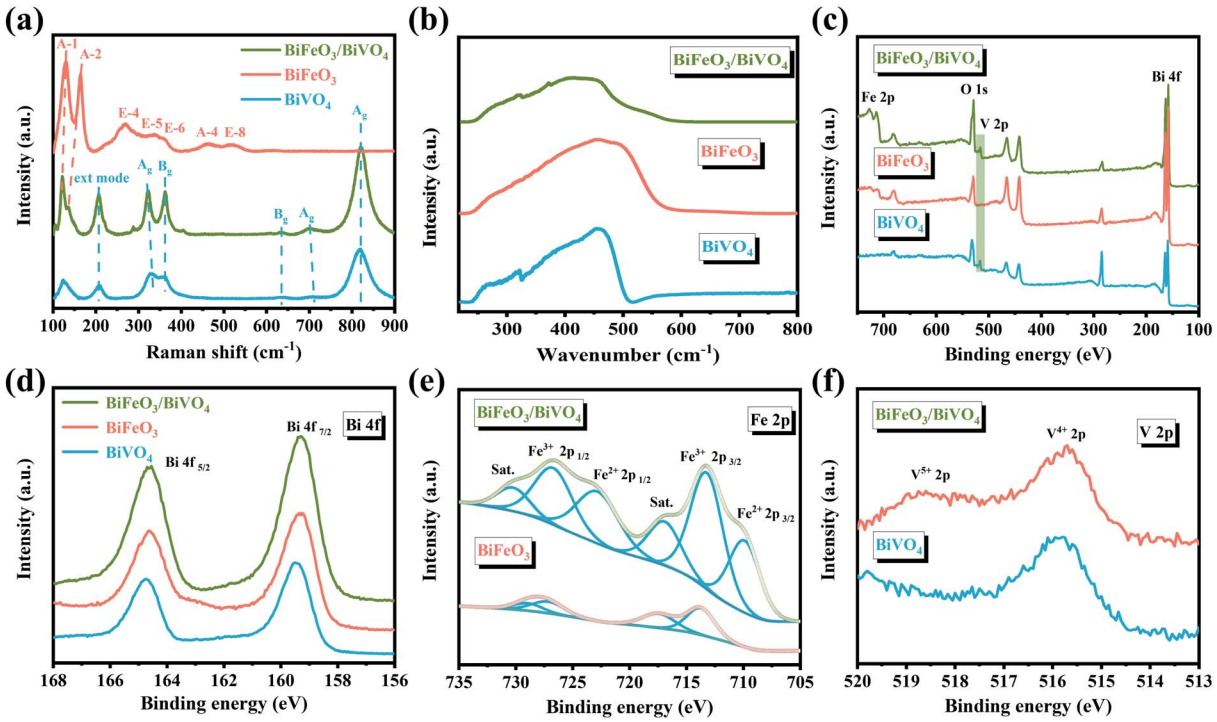

Fig. 4 (a) Raman spectra, (b) UV-Vis spectra, (c) XPS survey spectrum and (d) high-resolution Bi 4f spectrum of $BiFeO_3$, $BiVO_4$ and $BiFeO_3/BiVO_4$; (e) high-resolution Fe 2p spectrum of $BiFeO_3$ and $BiFeO_3/BiVO_4$; (f) high-resolution V 2p spectrum of $BiVO_4$ and $BiFeO_3/BiVO_4$.

Besides, two distinct peaks centered at 713.4 eV and 726.9 eV in the Fe 2p region can be attributed to the binding energies of Fe^{3+} $2p_{3/2}$ and Fe^{3+} $2p_{1/2}$, respectively (Fig. 4e).[55,56] And the XPS peak positioned at 515.8 eV in the V 2p spectrum illustrates the presence of V^{4+} (Fig. 4f). It is noteworthy that when $BiFeO_3$ was coupled with $BiVO_4$, the emerged new peaks in $BiFeO_3/BiVO_4$ hybrids are assigned to Fe^{2+} 2p and V^{5+} 2p peaks in contrast to pristine samples, elucidating that the apparent electronic interactions between $BiFeO_3$ and $BiVO_4$ domains are due to the formation of p–n heterojunctions.[57,58] More importantly, the related changes in the valence state further demonstrate that the charge transferred from $BiVO_4$ to $BiFeO_3$. All these results convincingly suggest the successful establishment of unique p–n heterojunctions and the transfer of electrons between $BiVO_4$ and $BiFeO_3$. The induced local charge redistribution contributes to the targeted adsorption of reactant molecules and thus enhances the electrocatalytic urea production ability.

The electrocatalytic activity of $BiFeO_3/BiVO_4$ hybrids for the C–N coupling reaction toward urea production was tested in a 0.1 M $KHCO_3$ solution utilizing an H-type two-compartment cell separated by a Nafion 211 membrane, which is equipped with a three-electrode configuration (Fig. S2†). Ultrahigh purity CO_2 gas (99.999%) and N_2 gas (99.999%) were continuously purged into the cathodic chamber with the same flow rate of 5 mL min^{-1} during the electrolysis process. The possibly generated liquid products (urea and NH_3) in the electrolytes were spectrophotometrically measured by the diacetyl monoxime method and indophenol blue method.[22,59] Meanwhile, the related calibration curves are displayed in Fig. S3.† Besides, online gas chromatography monitored the possible gas products such as CO and H_2. It has been reported that the electrochemical catalytic activity of the C–N coupling reaction for urea production was dominant as a result of effectively coupling the carbon dioxide reduction reaction (CO_2RR) with the nitrogen reduction reaction (NRR). As displayed in Fig. 5a and b, the $BiFeO_3/BiVO_4$ hybrids possess a high NH_3 faradaic efficiency (FE) (12.81%) for the NRR and CO FE (20.21%) for the CO_2RR, which establish the baseline of N_2 and CO_2 reduction activity. The linear sweep voltammetry curves (LSV) were initially examined in 0.1 M $KHCO_3$ saturated with different gas feeds (Ar, CO_2, N_2, or CO_2 + N_2). As depicted in Fig. 5c, the distinctly enhanced current density in CO_2 + N_2 saturated electrolyte relative to that in CO_2 and N_2, respectively, indicates the occurrence of the electrocatalytic C–N coupling reaction for urea production. A potentiostatic experiment was further performed to quantitatively assess the performance of electrocatalytic urea production of $BiFeO_3/BiVO_4$ hybrids at different working potentials. As shown in Fig. S4,† the corresponding chronoamperometry curves within the potential range of −0.3 V to −0.7 V exhibit stable current density after electrolysis for 2 h. As demonstrated in Fig. 5d, the urea yield rate and the corresponding FE increase with the increase of applied potential. The highest urea yield rate is 4.94 mmol h^{-1} g^{-1} with a FE of 17.18% at −0.4 *vs.* the reversible hydrogen electrode (RHE), outperforming all the reported values for Pd based catalysts (Table S1†). However, at more negative potentials, the electrocatalytic urea production performance decreases, which may result from the occupation of the active sites for N_2 and CO_2

© 2021 The Author(s). Published by the Royal Society of Chemistry

Open Access Article. Published on 12 April 2021. Downloaded on 09/11/2024 10:38:50 AM.
This article is licensed under a Creative Commons Attribution 3.0 Unported Licence.

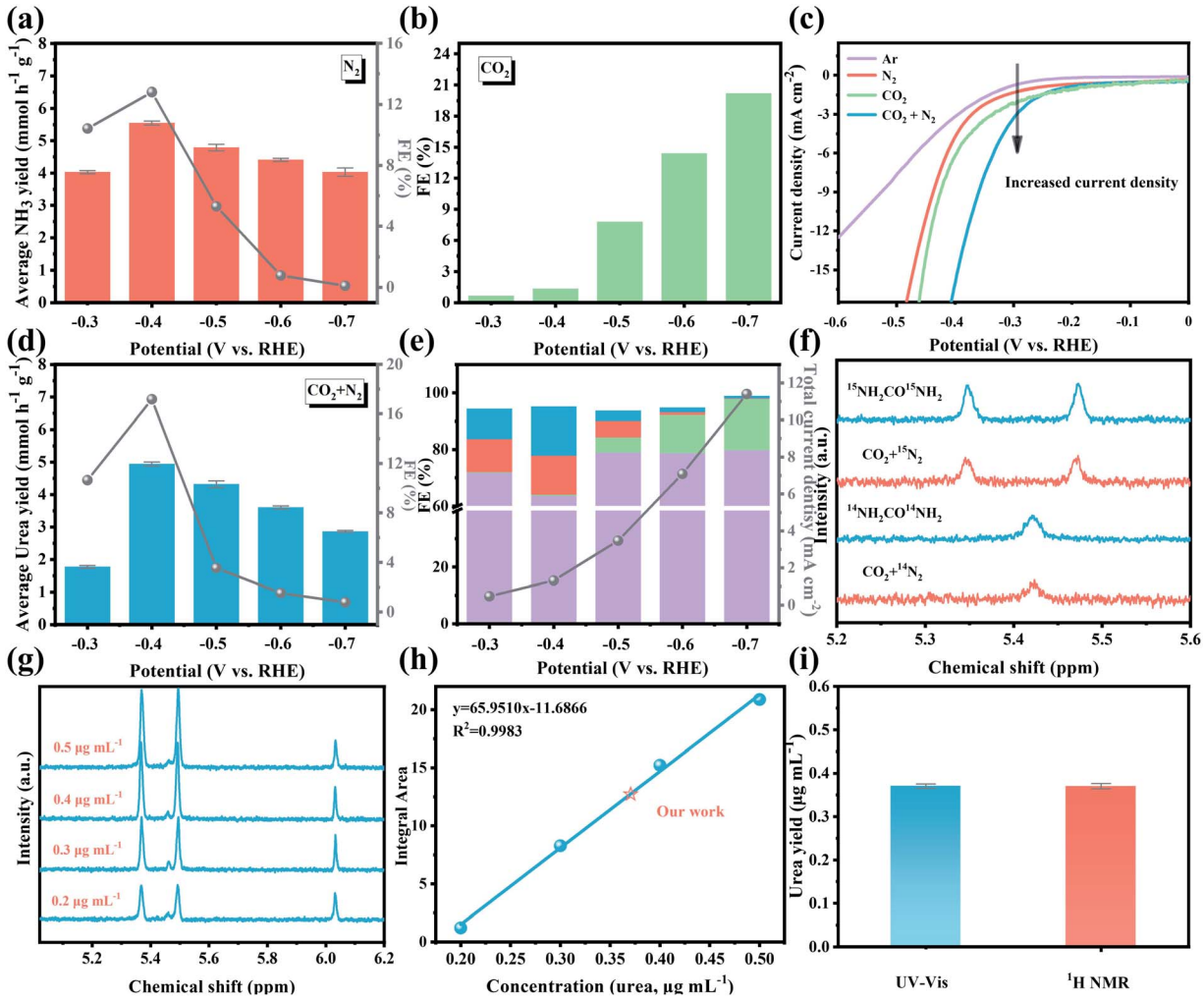

Fig. 5 (a) NH_3 synthesis with N_2 as the feed gas and (b) CO generation with CO_2 as the feed gas at various potentials for $BiFeO_3/BiVO_4$ hybrids; (c) LSV curves of $BiFeO_3/BiVO_4$ hybrids in Ar, N_2, CO_2 and N_2 + CO_2 saturated electrolyte; (d) the urea yield rate and faradaic efficiencies and (e) the corresponding product distribution of H_2 (purple color), CO (cyan-blue color), NH_3 (red color) and urea (blue color) for urea production with N_2 and CO_2 as the feed gas at various potentials for $BiFeO_3/BiVO_4$ hybrids; (f) ^{1}H NMR spectra of electrolyte saturated with $^{15}N_2$ + CO_2/$^{14}N_2$ + CO_2 after 2 h of electrolysis and standard $^{15}NH_2CO^{15}NH_2$/$^{14}NH_2CO^{14}NH_2$ solution; (g) ^{1}H NMR spectra of standard $^{15}NH_2CO^{15}NH_2$ solution at concentrations of 0.2–0.5 μg mL^{-1}; (h) integral area ($^{15}NH_2CO^{15}NH_2$/$C_4H_4O_4$)–concentration linear relation calibrated using standard $^{15}NH_2$-$CO^{15}NH_2$ solution; (i) the urea yield of $BiFeO_3/BiVO_4$ hybrids after 2 h of electrolysis determined using the UV-Vis spectrum and ^{1}H NMR spectra.

reduction by the excessively released CO (Fig. 5e). Additionally, the as-obtained $BiFeO_3/BiVO_4$ hybrids retain 96% of the initial current density after a 10 h long-term chronopotentiometry test (Fig. S5†). Likewise, when conducting five cycling tests, negligible change is observed in the electrocatalytic urea production performance (Fig. S6†), attesting to the superior electrocatalytic stability of $BiFeO_3/BiVO_4$ hybrids. The corresponding characterization studies further reveal that the $BiFeO_3/BiVO_4$ hybrids were well-matched with their original morphology, crystal phase, and chemical states after 10 h of continuous electrolysis (Fig. S7†), corroborating their robust structural stability. Impressively, with the aid of enhanced CO_2 adsorption capacity of an ionic liquid,[60] when the 1-butyl-3-methylimidazolium tetrafluoroborate–$KHCO_3$ ([Bmim]BF_4–$KHCO_3$) electrolyte was used in the system, a higher electrocatalytic activity for urea production is achieved (FE: 20.75%, urea yield rate: 5.42 mmol h^{-1} g^{-1}) than that obtained in pristine $KHCO_3$ solution at the same potential (Fig. S8†).

To gain solid proof that the produced urea originated from the C–N coupling reaction with CO_2 and N_2, a rigorous protocol was employed to avoid false-positive results caused by the contamination of environmental NO_X (Fig. S9†). Under all the control experiment conditions, negligible urea was detected, which excludes the possible effect of environmental NO_X on the urea electrosynthesis (Fig. S10†). $^{15}N_2$ isotopic labeling experiment was further utilized to corroborate the N source of the generated urea [$CO(NH_2)_2$]. The standard $CO(^{15}NH_2)_2$ sample displays two dominant peaks at approximately 5.35 ppm and 5.47 ppm in ^{1}H Nuclear Magnetic Resonance (NMR) (Fig. 5f), while the standard $CO(^{14}NH_2)_2$ sample possesses one distinct peak at about 5.42 ppm. When utilizing $^{15}N_2$ and CO_2 as the feed gas, the detected ^{1}H NMR signals of the produced urea

Open Access Article. Published on 12 April 2021. Downloaded on 09/11/2024 10:38:50 AM.
This article is licensed under a Creative Commons Attribution 3.0 Unported Licence.

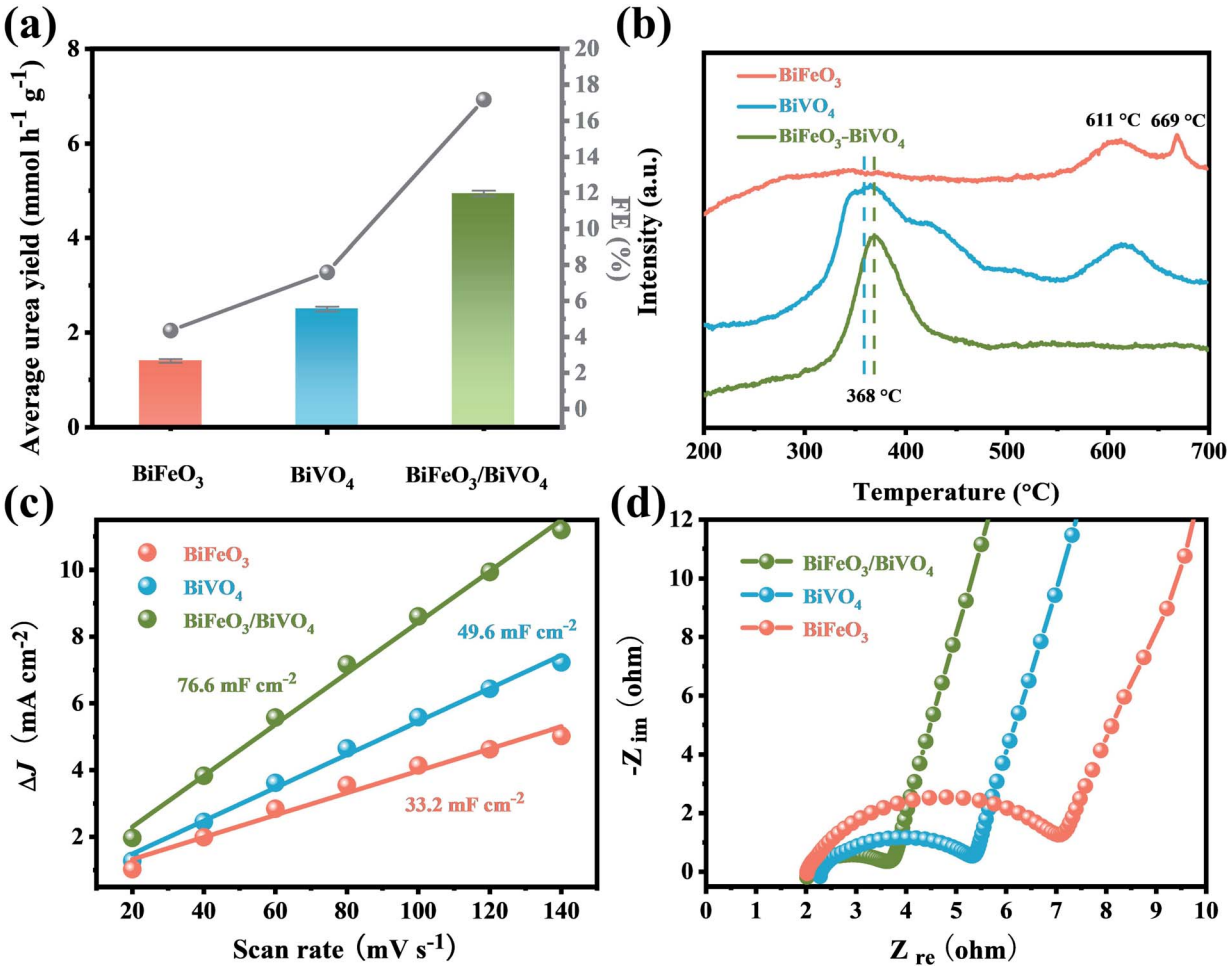

Fig. 6 (a) Average urea yield; (b) carbon dioxide temperature-programmed desorption (CO_2-TPD) spectra; (c) ΔJ of electrocatalysts plotted against scan rate at −0.05 V *vs.* RHE; (d) Nyquist plots of electrochemical impedance spectra (EIS) of $BiFeO_3$, $BiVO_4$ and $BiFeO_3/BiVO_4$.

matched well with the standard $CO(^{15}NH_2)_2$ signals. Additionally, the concentration of $CO(^{15}NH_2)_2$ was also quantitatively detected by ^1H NMR, and the related signal integration–concentration linear relation is exhibited in Fig. 5g and h. As expected, the calculated urea concentration is consistent with the quantitative results of the diacetyl monoxime method (Fig. 5i). All these results are convincingly indicative of urea originating from the C–N coupling reaction from N_2 and CO_2 catalyzed by $BiFeO_3/BiVO_4$ hybrids.

For comparison, the pristine $BiFeO_3$ and $BiVO_4$ were also evaluated under identical conditions. At the optimal potential of −0.4 V, the electrocatalytic activities of $BiFeO_3$ (urea yield rate: 1.41 mmol h^{-1} g^{-1}, FE: 4.35%) and $BiVO_4$ (urea yield rate: 2.50 mmol h^{-1} g^{-1}, FE: 7.59%) were much inferior to those of $BiFeO_3/BiVO_4$ hybrids for urea production (Fig. 6a). This indicates that the local charge redistribution in $BiFeO_3/BiVO_4$ hybrids plays a critical role in enhancing electrocatalytic urea production. As revealed by temperature-programmed desorption (TPD), compared with pristine $BiFeO_3$ and $BiVO_4$, $BiFeO_3/BiVO_4$ hybrids exhibited stronger binding strength and larger desorption peak in the CO_2- and N_2-TPD spectra (Fig. 6b and S11†), elucidating that the local charge redistribution in $BiFeO_3/BiVO_4$ hybrids endows the surfaces of $BiFeO_3$ and $BiVO_4$ with local nucleophilic and electrophilic regions and thus promotes the targeted adsorption of CO_2 and N_2 molecules, which is in good agreement with the aforementioned theoretical prediction. The electrochemically active surface area (ECSA) results suggest that the $BiFeO_3/BiVO_4$ hybrids (76.6 mF cm^{-2}) display a higher electrochemical double-layer capacitance (C_{dl}) than pristine $BiFeO_3$ (33.2 mF cm^{-2}) and $BiVO_4$ (49.6 mF cm^{-2}), which signifies that local charge redistribution promotes the exposure of more active sites in $BiFeO_3/BiVO_4$ hybrids for gas molecule adsorption and activation (Fig. 6c and S12†). Electrochemical impedance spectroscopy (EIS) analysis further reveals that the $BiFeO_3/BiVO_4$ hybrids possess a smaller semicircle and higher slope than pristine samples, evincing that the presence of local charge redistribution in $BiFeO_3/BiVO_4$ hybrids significantly promotes electron/ion transfer kinetics during the electrocatalytic process (Fig. 6d).[29,43]

To obtain deeper insight into the C–N coupling reaction mechanism toward the electrocatalytic urea production, DFT calculation was further employed to assess the intermediate variation and energy barrier during the reaction process. The corresponding $BiFeO_3/BiVO_4$ heterostructured architecture is

© 2021 The Author(s). Published by the Royal Society of Chemistry

Open Access Article. Published on 12 April 2021. Downloaded on 09/11/2024 10:38:50 AM.
This article is licensed under a Creative Commons Attribution 3.0 Unported Licence.

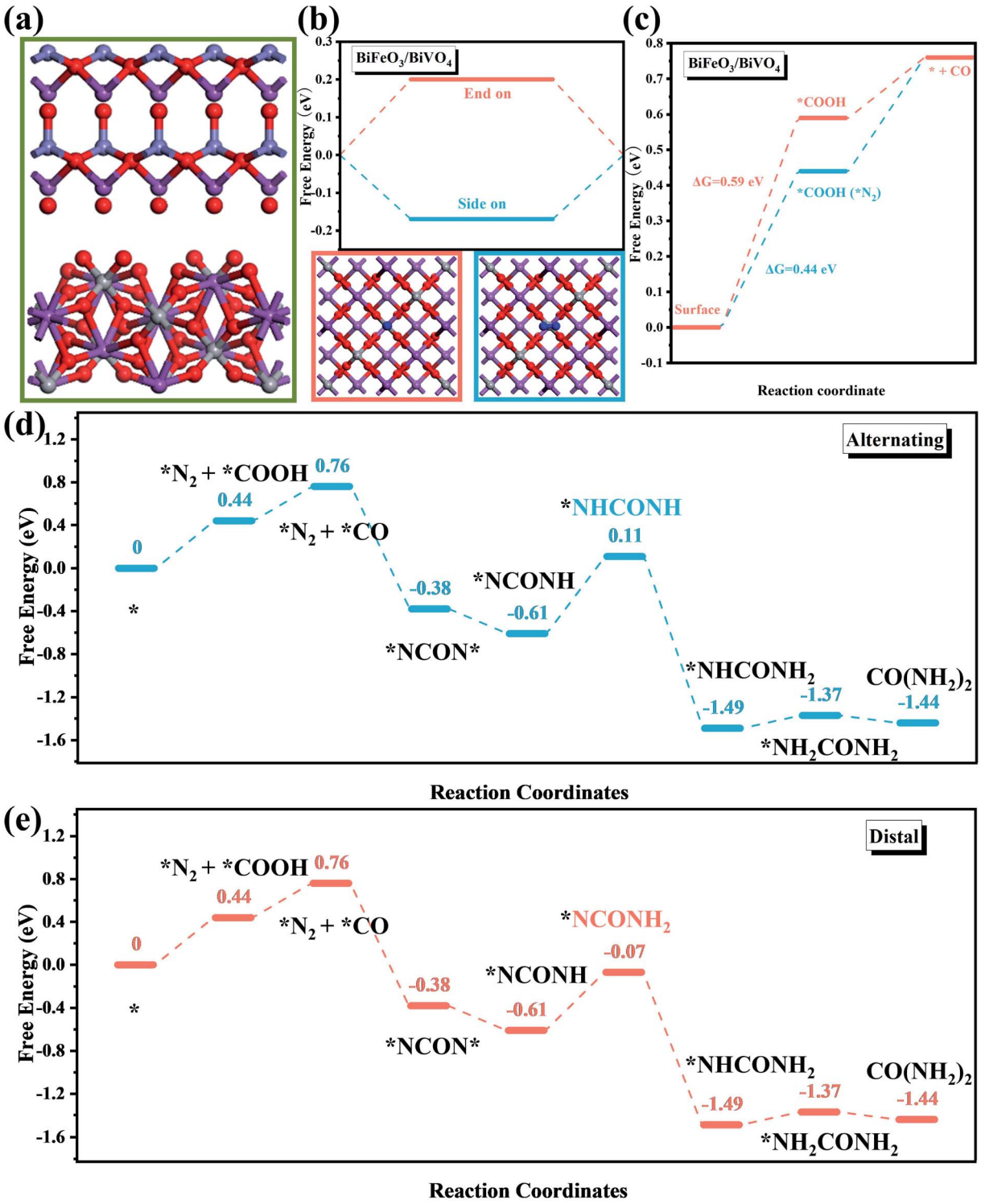

Fig. 7 (a) The calculation model of the $BiFeO_3/BiVO_4$ heterostructure; free energy diagrams for (b) N_2 adsorption and (c) CO_2 reduction with and without N_2 adsorption on the $BiFeO_3/BiVO_4$ heterostructure; the electrolytic urea production *via* (d) alternating and (e) distal mechanisms.

displayed in Fig. 7a. Since the chemisorption of inert CO_2 and N_2 molecules is the initial step for electrocatalytic urea production, it is critical to reveal the competitive adsorption between these gas molecules. In comparison with CO_2-TPD, the peaks in the N_2-TPD spectrum of the heterostructured hybrids appeared at a higher temperature and exhibited enhanced intensity, demonstrating that the $BiFeO_3/BiVO_4$ hybrids possessed stronger N_2 chemisorption ability than that for CO_2 molecules (Fig. 6c and S11†).[9] In other words, the C–N coupling reaction was initiated with chemisorption of N_2 molecules on

Open Access Article. Published on 12 April 2021. Downloaded on 09/11/2024 10:38:50 AM.
This article is licensed under a Creative Commons Attribution 3.0 Unported Licence.

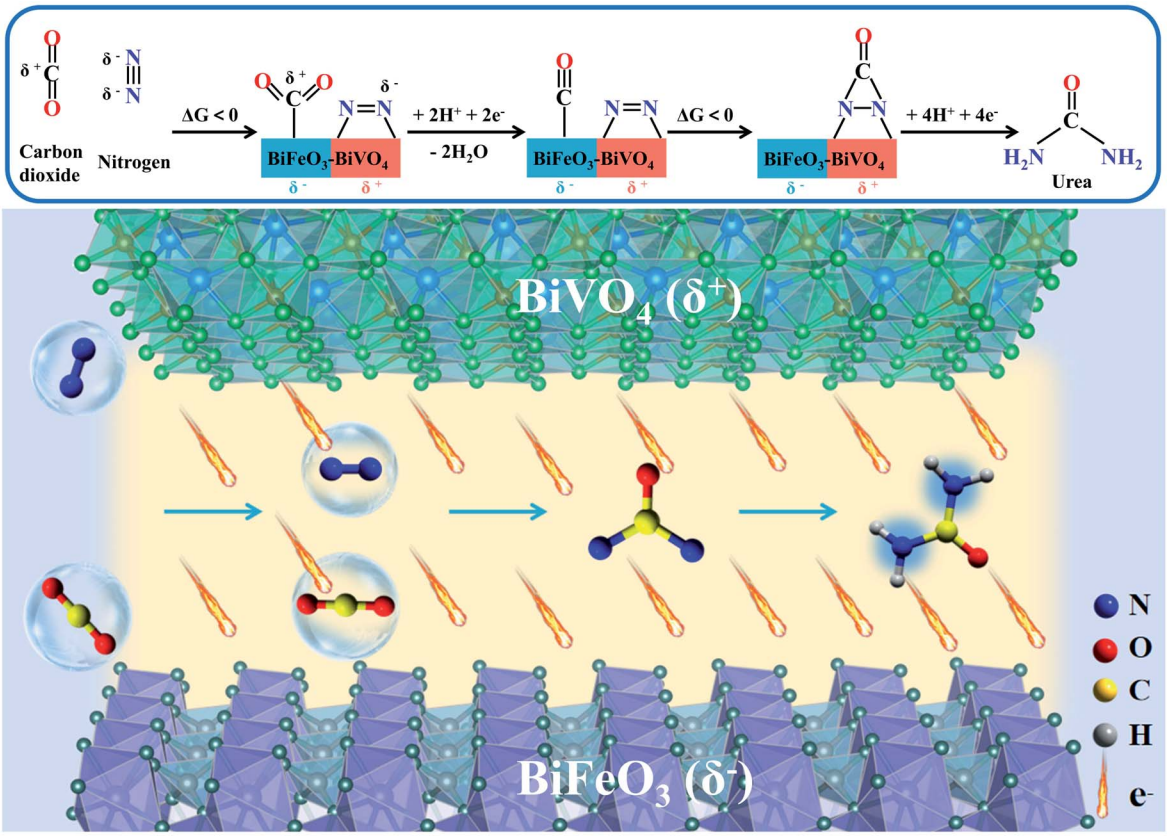

Fig. 8 The schematic electrocatalytic urea production mechanism based on $BiFeO_3/BiVO_4$ p–n heterostructure synergistic effects.

the $BiFeO_3/BiVO_4$ hybrids. Besides, the free energy of the N_2 adsorption with a side-on configuration was more negative than that of an end-on configuration, suggesting that N_2 preferably adsorbed on the local electrophilic $BiVO_4$ regions *via* the more stable side-on configuration (Fig. 7b). Impressively, as identified in Fig. 7c, the $BiFeO_3/BiVO_4$ hybrids required the highest Gibbs free energy (ΔG) of 0.59 eV to reduce CO_2, while the ΔG decreased to 0.44 eV when the N_2 molecules emerged in neighboring $BiVO_4$ regions. Therefore, it can be deduced that the adsorbed/activated N_2 molecules would facilitate the reduction of adsorbed CO_2 to CO on local nucleophilic $BiFeO_3$ regions. Then the C–N coupling reaction spontaneously occurred between the activated N_2 molecules (*N=N*) and *in situ* generated CO to form the *NCON* intermediate, due to the matching molecular orbitals. The corresponding ΔG further corroborates that the formation of the *NCON* intermediate is an exothermic process. Once the *NCON* intermediate is generated, the subsequent hydrogenation of *NCON* would produce two possible reaction pathways involving distal and alternating mechanisms. Concerning the alternating pathway, the $(H^+ + e^-)$ alternately reacted with the two N atoms, while the protonation continuously attacked the distal N atoms for the distal mechanism. As displayed in Fig. 7d and e, when the reduction of *NCON* follows the distal pathway, the required ΔG decreased to 0.54 eV compared to that of the alternating pathway (0.72 eV), suggesting that the $BiFeO_3/BiVO_4$ hybrids were prone to pursue the distal mechanism until the release of urea molecules rather than the alternating pathway from the thermodynamic perspective.[31]

The selectivity of the electrocatalytic urea production is closely associated with the formation of *NCON* intermediates. The possible N_2 reduction or the excessive release of CO would result in a decrease in the efficiency of the electrocatalytic C–N coupling reaction and further reduce the selectivity. On the one hand, the ΔG for the reductive protonation of $*N_2$ into $*N_2H$ ($N_2 + H^+ + e^- + * \rightarrow *NNH$), which is regarded as the potential-determining step (PDS) toward the NRR, was calculated to be 0.14 eV (Fig. S13†),[61] which was much higher than that for the C–N coupling reaction to form *NCON*. Such a significantly larger energy barrier makes $BiFeO_3/BiVO_4$ hybrids inactive for the electrocatalytic NRR, let alone generating side product NH_3. On the other hand, the release of the generated *CO intermediate was strongly associated with the selectivity of the electrocatalytic urea production. Thus, the stability of the as-prepared electrocatalysts against CO poisoning was evaluated through an electrochemical CO-stripping experiment. As shown in Fig. S14,† the CO-stripping peak of $BiFeO_3/BiVO_4$ hybrids (0.251 V *vs.* RHE) exhibits a more negative shift than that of pristine $BiFeO_3$ (0.261 V *vs.* RHE) and $BiVO_4$ counterparts (0.265 V *vs.* RHE), indicating that the $BiFeO_3/BiVO_4$ hybrids possessed higher stability against CO poisoning, which is due to the elimination of some of the strong adsorption sites by the

© 2021 The Author(s). Published by the Royal Society of Chemistry

Open Access Article. Published on 12 April 2021. Downloaded on 09/11/2024 10:38:50 AM. This article is licensed under a Creative Commons Attribution 3.0 Unported Licence.

local charge redistribution.[62] Notably, the amount of CO should be well controlled. As confirmed by Fig. 5e, when the applied potential exceeded −0.4 V, the excessively released CO occupied the adsorption sites for N_2 and CO_2 and resulted in a remarkable decrease of the FE for urea production.

By combining the aforementioned experimental results and computational simulations, the overall urea electrosynthesis process can be summarized in the following steps: (i) the built-in electric field in $BiFeO_3$/$BiVO_4$ hybrids accelerates the local charge redistribution, (ii) N_2/CO_2 molecules first adsorbed on the generated electrophilic/nucleophilic regions by electrostatic interaction, (iii) the produced $*N_2$ promotes CO_2 reduction under the electric field, and then the generated CO will further react with $*N_2$ to produce the desirable *NCON* intermediate through exothermic electrocatalytic C–N coupling reaction, and (iv) the subsequent protonation process preferentially undergoes the distal mechanism until the formation of urea (Fig. 8).

3 Conclusion

In summary, inspired by the theoretical simulation predictions, a facile ultrasonic bath strategy was proposed to elaborately integrate the perovskite structured $BiFeO_3$ and $BiVO_4$ as a unique p–n heterojunction. The well-developed built-in electric field at the heterointerfaces facilitates the local charge redistribution and thus endows the $BiFeO_3$ and $BiVO_4$ surfaces with local nucleophilic and electrophilic regions, which promote the targeted adsorption and activation of N_2 and CO_2 molecules. Besides, the local charge redistribution also contributed to fully exposing the active sites and accelerated electrocatalytic kinetics, which is beneficial for the formation of the C–N bond and generation of the desired *NCON* intermediate. As a result, the $BiFeO_3$/$BiVO_4$ hybrids exhibit a maximum urea yield rate and FE of 4.94 mmol h^{-1} g^{-1} and 17.18% at −0.4 V *vs.* RHE in 0.1 M $KHCO_3$. Besides, the related urea yield rate and FE can be further improved to 5.42 mmol h^{-1} g^{-1} and 20.75% in (Bmim)BF_4–$KHCO_3$ electrolyte. This work proposed an innovative local charge redistribution concept to design urea production catalysts by promoting electrocatalytic C–N bond coupling.

Author contributions

The manuscript was written through contributions of all authors. All authors have given approval to the final version of the manuscript.

Conflicts of interest

There are no conflicts to declare.

Acknowledgements

This work is supported by the National Key R&D Program of China (No. 2020YFA0710200) and the Chemistry and Chemical Engineering Guangdong Laboratory (No. 1922006). We also thank the financial project of the Key Program for International S&T Cooperation Projects (No. 2018YFE0124600) funded by the Ministry of Science and Technology of China.

References

1 J. W. Erisman, M. A. Sutton, J. Galloway, Z. Klimont and W. Winiwarter, *Nat. Geosci.*, 2008, **1**, 636–639.
2 K. C. MacLeod and P. L. Holland, *Nat. Chem.*, 2013, **5**, 559–565.
3 H.-P. Jia and E. A. Quadrelli, *Chem. Soc. Rev.*, 2014, **43**, 547–564.
4 P. Lu, D. Gao, H. He, Q. Wang, Z. Liu, S. Dipazir, M. Yuan, W. Zu and G. Zhang, *Nanoscale*, 2019, **11**, 7805–7812.
5 T.-T. Zhuang, Y. Pang, Z.-Q. Liang, Z. Wang, Y. Li, C.-S. Tan, J. Li, C. T. Dinh, P. De Luna, P.-L. Hsieh, T. Burdyny, H.-H. Li, M. Liu, Y. Wang, F. Li, A. Proppe, A. Johnston, D.-H. Nam, Z.-Y. Wu, Y.-R. Zheng, A. H. Ip, H. Tan, L.-J. Chen, S.-H. Yu, S. O. Kelley, D. Sinton and E. H. Sargent, *Nat. Catal.*, 2018, **1**, 946–951.
6 S. Nitopi, E. Bertheussen, S. B. Scott, X. Liu, A. K. Engstfeld, S. Horch, B. Seger, I. E. L. Stephens, K. Chan, C. Hahn, J. K. Nørskov, T. F. Jaramillo and I. Chorkendorff, *Chem. Rev.*, 2019, **119**, 7610–7672.
7 Z.-Q. Liang, T.-T. Zhuang, A. Seifitokaldani, J. Li, C.-W. Huang, C.-S. Tan, Y. Li, P. De Luna, C. T. Dinh, Y. Hu, Q. Xiao, P.-L. Hsieh, Y. Wang, F. Li, R. Quintero-Bermudez, Y. Zhou, P. Chen, Y. Pang, S.-C. Lo, L.-J. Chen, H. Tan, Z. Xu, S. Zhao, D. Sinton and E. H. Sargent, *Nat. Commun.*, 2018, **9**, 3828.
8 Z. Lyu, S. Zhu, M. Xie, Y. Zhang, Z. Chen, R. Chen, M. Tian, M. Chi, M. Shao and Y. Xia, *Angew. Chem., Int. Ed.*, 2021, **60**, 1909–1915.
9 C. Chen, X. Zhu, X. Wen, Y. Zhou, L. Zhou, H. Li, L. Tao, Q. Li, S. Du, T. Liu, D. Yan, C. Xie, Y. Zou, Y. Wang, R. Chen, J. Huo, Y. Li, J. Cheng, H. Su, X. Zhao, W. Cheng, Q. Liu, H. Lin, J. Luo, J. Chen, M. Dong, K. Cheng, C. Li and S. Wang, *Nat. Chem.*, 2020, **12**, 717–724.
10 D. Gao, R. M. Arán-Ais, H. S. Jeon and B. Roldan Cuenya, *Nat. Catal.*, 2019, **2**, 198–210.
11 D. M. Weekes, D. A. Salvatore, A. Reyes, A. Huang and C. P. Berlinguette, *Acc. Chem. Res.*, 2018, **51**, 910–918.
12 X. Li, T. Li, Y. Ma, Q. Wei, W. Qiu, H. Guo, X. Shi, P. Zhang, A. M. Asiri, L. Chen, B. Tang and X. Sun, *Adv. Energy Mater.*, 2018, **8**, 1801357.
13 N. Zhang, A. Jalil, D. Wu, S. Chen, Y. Liu, C. Gao, W. Ye, Z. Qi, H. Ju, C. Wang, X. Wu, L. Song, J. Zhu and Y. Xiong, *J. Am. Chem. Soc.*, 2018, **140**, 9434–9443.
14 Y. Liu, M. Cheng, Z. He, B. Gu, C. Xiao, T. Zhou, Z. Guo, J. Liu, H. He, B. Ye, B. Pan and Y. Xie, *Angew. Chem., Int. Ed.*, 2019, **58**, 731–735.
15 H. B. Yang, S.-F. Hung, S. Liu, K. Yuan, S. Miao, L. Zhang, X. Huang, H.-Y. Wang, W. Cai, R. Chen, J. Gao, X. Yang, W. Chen, Y. Huang, H. M. Chen, C. M. Li, T. Zhang and B. Liu, *Nat. Energy*, 2018, **3**, 140–147.

Open Access Article. Published on 12 April 2021. Downloaded on 09/11/2024 10:38:50 AM. This article is licensed under a Creative Commons Attribution 3.0 Unported Licence.

16 P. Lu, J. Zhang, H. He, M. Wang, Z. Luo, D. Gao, Z. Liu, X. Wang, M. Yuan, S. Dipazir, H. Zhao, Y. Xie and G. Zhang, *J. Power Sources*, 2020, **449**, 227496.
17 X. Cui, C. Tang and Q. Zhang, *Adv. Energy Mater.*, 2018, **8**, 1800369.
18 P. M. Glibert, R. Maranger, D. J. Sobota and L. Bouwman, *Environ. Res. Lett.*, 2014, **9**, 105001.
19 M. Boota and Y. Gogotsi, *Adv. Energy Mater.*, 2019, **9**, 1802917.
20 C. Tang and S.-Z. Qiao, *Chem. Soc. Rev.*, 2019, **48**, 3166–3180.
21 C. J. M. van der Ham, M. T. M. Koper and D. G. H. Hetterscheid, *Chem. Soc. Rev.*, 2014, **43**, 5183–5191.
22 M. Yuan, Q. Li, J. Zhang, J. Wu, T. Zhao, Z. Liu, L. Zhou, H. He, B. Li and G. Zhang, *Adv. Funct. Mater.*, 2020, **30**, 2004208.
23 S. H. Lee, J. C. Lin, M. Farmand, A. T. Landers, J. T. Feaster, J. E. Aviles Acosta, J. W. Beeman, Y. Ye, J. Yano, A. Mehta, R. C. Davis, T. F. Jaramillo, C. Hahn and W. S. Drisdell, *J. Am. Chem. Soc.*, 2020, **143**, 588–592.
24 F. Hu, S. C. Abeyweera, J. Yu, D. Zhang, Y. Wang, Q. Yan and Y. Sun, *Chem*, 2020, **6**, 3007–3021.
25 H. Cheng, S. Liu, J. Zhang, T. Zhou, N. Zhang, X.-s. Zheng, W. Chu, Z. Hu, C. Wu and Y. Xie, *Nano Lett.*, 2020, **20**, 6097–6103.
26 X. Zhang, Y. Wang, M. Gu, M. Wang, Z. Zhang, W. Pan, Z. Jiang, H. Zheng, M. Lucero, H. Wang, G. E. Sterbinsky, Q. Ma, Y.-G. Wang, Z. Feng, J. Li, H. Dai and Y. Liang, *Nat. Energy*, 2020, **5**, 684–692.
27 H. S. Kim, J. Choi, J. Kong, H. Kim, S. J. Yoo and H. S. Park, *ACS Catal.*, 2021, **11**, 435–445.
28 S. Wang, L. Shi, X. Bai, Q. Li, C. Ling and J. Wang, *ACS Cent. Sci.*, 2020, **6**, 1762–1771.
29 M. Yuan, Y. Bai, J. Zhang, T. Zhao, S. Li, H. He, Z. Liu, Z. Wang and G. Zhang, *J. Mater. Chem. A*, 2020, **8**, 26066–26074.
30 M. Yuan, H. Zhang, D. Gao, H. He, Y. Sun, P. Lu, S. Dipazir, Q. Li, L. Zhou, S. Li, Z. Liu, J. Yang, Y. Xie, H. Zhao and G. Zhang, *J. Mater. Chem. A*, 2020, **8**, 2691–2700.
31 M. Yuan, J. Chen, Y. Bai, Z. Liu, J. Zhang, T. Zhao, Q. Wang, S. Li, H. He and G. Zhang, *Angew. Chem., Int. Ed.*, 2021, DOI: 10.1002/anie.202101275.
32 M. Jouny, G. S. Hutchings and F. Jiao, *Nat. Catal.*, 2019, **2**, 1062–1070.
33 J. Qiao, Y. Liu, F. Hong and J. Zhang, *Chem. Soc. Rev.*, 2014, **43**, 631–675.
34 M. Aresta, A. Dibenedetto and A. Angelini, *Chem. Rev.*, 2014, **114**, 1709–1742.
35 D. B. Kayan and F. Köleli, *Appl. Catal., B*, 2016, **181**, 88–93.
36 A. R. Singh, B. A. Rohr, J. A. Schwalbe, M. Cargnello, K. Chan, T. F. Jaramillo, I. Chorkendorff and J. K. Nørskov, *ACS Catal.*, 2017, **7**, 706–709.
37 H. Wang, Y. Li, C. Li, K. Deng, Z. Wang, Y. Xu, X. Li, H. Xue and L. Wang, *J. Mater. Chem. A*, 2019, **7**, 801–805.
38 H. Cui, B. Li, Y. Zhang, X. Zheng, X. Li, Z. Li and S. Xu, *Int. J. Hydrogen Energy*, 2018, **43**, 18242–18252.
39 N. Tsvetkov, Q. Lu, L. Sun, E. J. Crumlin and B. Yildiz, *Nat. Mater.*, 2016, **15**, 1010–1016.
40 K. He, T. T. Tsega, X. Liu, J. Zai, X.-H. Li, X. Liu, W. Li, N. Ali and X. Qian, *Angew. Chem., Int. Ed.*, 2019, **58**, 11903–11909.
41 Y. Lin, C. Yang, S. Wu, X. Li, Y. Chen and W. L. Yang, *Adv. Funct. Mater.*, 2020, **30**, 2002918.
42 X. Ning, Y. Wu, X. Ma, Z. Zhang, R. Gao, J. Chen, D. Shan and X. Lu, *Adv. Funct. Mater.*, 2019, **29**, 1902992.
43 M. Yuan, S. Dipazir, M. Wang, Y. Sun, D. Gao, Y. Bai, M. Zhang, P. Lu, H. He, X. Zhu, S. Li, Z. Liu, Z. Luo and G. Zhang, *J. Mater. Chem. A*, 2019, **7**, 3317–3326.
44 A. Sivanantham, P. Ganesan and S. Shanmugam, *Appl. Catal., B*, 2018, **237**, 1148–1159.
45 M. O. Ramirez, M. Krishnamurthi, S. Denev, A. Kumar, S.-Y. Yang, Y.-H. Chu, E. Saiz, J. Seidel, A. P. Pyatakov, A. Bush, D. Viehland, J. Orenstein, R. Ramesh and V. Gopalan, *Appl. Phys. Lett.*, 2008, **92**, 022511.
46 G. L. Yuan, S. W. Or and H. L. W. Chan, *J. Appl. Phys.*, 2007, **101**, 064101.
47 Y. K. Kho, W. Y. Teoh, A. Iwase, L. Mädler, A. Kudo and R. Amal, *ACS Appl. Mater. Interfaces*, 2011, **3**, 1997–2004.
48 L. Sandhya Kumari, P. Prabhakar Rao, A. Narayana Pillai Radhakrishnan, V. James, S. Sameera and P. Koshy, *Sol. Energy Mater. Sol. Cells*, 2013, **112**, 134–143.
49 F. D. Hardcastle and I. E. Wachs, *J. Phys. Chem.*, 1991, **95**, 5031–5041.
50 W. Wei, H. Xuan, L. Wang, Y. Zhang, K. Shen, D. Wang, T. Qiu and Q. Xu, *Phys. B*, 2012, **407**, 2243–2246.
51 T. Zhou, W. Xu, N. Zhang, Z. Du, C. Zhong, W. Yan, H. Ju, W. Chu, H. Jiang, C. Wu and Y. Xie, *Adv. Mater.*, 2019, **31**, 1807468.
52 S. Tosonian, C. J. Ruiz, A. Rios, E. Frias and J. F. Eichler, *Open J. Inorg. Chem.*, 2013, **3**, 7–13.
53 K.-H. Ye, X. Yu, Z. Qiu, Y. Zhu, X. Lu and Y. Zhang, *RSC Adv.*, 2015, **5**, 34152–34156.
54 S. Xie, T. Zhai, Y. Zhu, W. Li, R. Qiu, Y. Tong and X. Lu, *Int. J. Hydrogen Energy*, 2014, **39**, 4820–4827.
55 M. Balamurugan, G. Yun, K.-S. Ahn and S. H. Kang, *J. Phys. Chem. C*, 2017, **121**, 7625–7634.
56 T. Soltani, A. Tayyebi and B.-K. Lee, *Catal. Today*, 2020, **340**, 188–196.
57 Y. Yang, Y. Kang, H. Zhao, X. Dai, M. Cui, X. Luan, X. Zhang, F. Nie, Z. Ren and W. Song, *Small*, 2020, **16**, 1905083.
58 Y. Lin, K. Sun, S. Liu, X. Chen, Y. Cheng, W.-C. Cheong, Z. Chen, L. Zheng, J. Zhang, X. Li, Y. Pan and C. Chen, *Adv. Energy Mater.*, 2019, **9**, 1901213.
59 M. Rahmatullah and T. R. C. Boyde, *Clin. Chim. Acta*, 1980, **107**, 3–9.
60 M. Alvarez-Guerra, J. Albo, E. Alvarez-Guerra and A. Irabien, *Energy Environ. Sci.*, 2015, **8**, 2574–2599.
61 E. Skúlason, T. Bligaard, S. Gudmundsdóttir, F. Studt, J. Rossmeisl, F. Abild-Pedersen, T. Vegge, H. Jónsson and J. K. Nørskov, *Phys. Chem. Chem. Phys.*, 2012, **14**, 1235–1245.
62 W. Zhang, Y. Yang, B. Huang, F. Lv, K. Wang, N. Li, M. Luo, Y. Chao, Y. Li, Y. Sun, Z. Xu, Y. Qin, W. Yang, J. Zhou, Y. Du, D. Su and S. Guo, *Adv. Mater.*, 2019, **31**, 1805833.

© 2021 The Author(s). Published by the Royal Society of Chemistry